Research Article

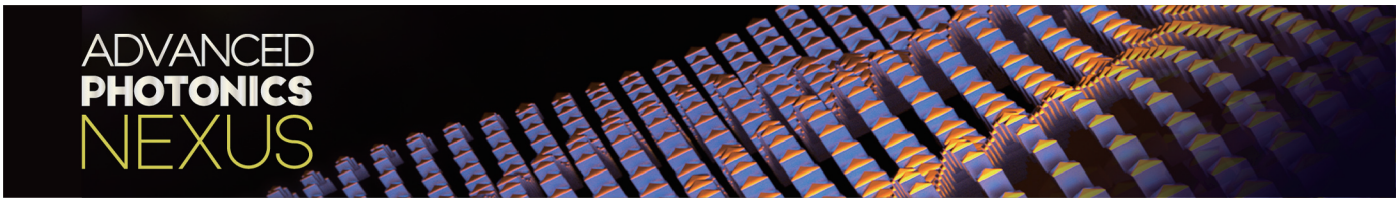

Highly efficient second-harmonic generation in a double-layer thin-film lithium niobate waveguide

Yuan Li,[a] Xiuquan Zhang,[b] Lutong Cai,[a,*] and Lin Zhang[a,c,*]

[a]Tianjin University, School of Precision Instruments and Opto-Electronics Engineering, State Key Laboratory of Precision Measuring Technology and Instruments, Key Laboratory of Opto-Electronic Information Technology of Ministry of Education, Tianjin Key Laboratory of Integrated Opto-Electronics Technologies and Devices, Tianjin, China

[b]Shandong University, Ministry of Education, Key Laboratory of Laser and Infrared System, Qingdao, China

[c]Peng Cheng Laboratory, Shenzhen, China

Abstract. Thin-film lithium niobate (LN) has emerged as an ideal platform for efficient nonlinear wave-mixing processes due to its strong quadratic nonlinearity and high optical confinement. We demonstrate unprecedentedly efficient second-harmonic generation (SHG) in a double-layer thin-film LN waveguide. The modal overlap between fundamental and second-harmonic waves is significantly enhanced by the polarization-reversed double layers, leading to a normalized conversion efficiency higher than 10,000% $W^{-1}\,cm^{-2}$ in theory. Under the low- and high-power pumping conditions, the measured normalized and absolute conversion efficiencies are 9600% $W^{-1}\,cm^{-2}$ and 85%, respectively, substantially higher than state-of-the-art values among the reported SHGs in thin-film LN waveguides. Our results hold great promise for the development of efficient and scalable nonlinear photonic devices, with applications including metrology and quantum information processing.

Keywords: integrated optics; second-harmonic generation; lithium niobate.

Received Jul. 5, 2024; revised manuscript received Sep. 19, 2024; accepted for publication Oct. 21, 2024; published online Nov. 7, 2024.

[DOI: 10.1117/1.APN.3.6.066009]

1 Introduction

Quadratic nonlinearity ($\chi^{(2)}$) is the basis of many important nonlinear optical processes,[1] such as second-harmonic generation (SHG), sum-frequency generation, difference-frequency generation, optical parametric oscillation, and nonclassical spontaneous parametric downconversion, making it very promising in a broad range of applications, including wavelength conversion, frequency metrology, and quantum information processing.[2–5] Among the materials possessing $\chi^{(2)}$ nonlinearity, lithium niobate (LN), a multifunctional ferroelectric crystal with excellent properties including low absorption loss, a wide transparent window ($0.35-5\ \mu m$), a high electro-optic coefficient ($r_{33}\sim 34$ pm/V), and strong second-order nonlinearity ($d_{33}\sim 25$ pm/V), plays an important role in nonlinear and quantum optics.[6] Efficient wavelength conversion in LN waveguides typically relies on periodically poled lithium niobate (PPLN) to achieve quasi-phase matching (QPM).[7] However, these nonlinear photonic devices based on bulk LN suffer from large footprints and low conversion efficiencies due to the relatively large optical mode areas in proton-exchanged and titanium-diffused waveguides.[8,9]

Recently, LN-on-insulator (LNOI) technology has attracted considerable attention because the high refractive index contrast between the core and cladding leads to strong optical confinement, making it possible to achieve high-density photonic integration and efficient nonlinear interaction.[10–12] To date, the LNOI platform has hosted a wide variety of high-performance photonic devices, including high-speed electro-optic modulators, efficient acousto-optic frequency shifters, and high-gain chip-scale amplifiers.[13–15] In addition, the enhanced second-order nonlinear interaction could considerably improve the wave-mixing efficiencies in various nonlinear optical processes.[16–20]

As a mainstream approach for SHG using LN, the QPM scheme has been successfully implemented in a hybrid silicon nitride–LNOI waveguide with a normalized conversion efficiency (η_{norm}) of 160% $W^{-1}\,cm^{-2}$ in 2016.[21] It is significantly improved to higher than 2000% $W^{-1}\,cm^{-2}$ in periodically poled

*Address all correspondence to Lutong Cai, lutong_cai@tju.edu.cn; Lin Zhang, lin_zhang@tju.edu.cn

LNOI (PPLNOI) waveguides, although it is still lower than the theoretical value, possibly due to imperfect domain poling.[22–25] Moreover, achieving uniform domain inversion faces great challenges for on-chip LNOI devices that require small domain poling periods, especially for generating short-wavelength light (e.g., blue and ultraviolet lights), since the random domain growth and leakage currents can result in poor poling quality.[26] Many efforts were then made in improving the poling process,[27] such as actively monitoring the poling process and adapted poling approach, achieving a η_{norm} of up to 4600% $\text{W}^{-1}\,\text{cm}^{-2}$ for SHG in a 0.6-mm-long waveguide[28] and an absolute conversion efficiency (η_{abs}) of 82.5% for a 21-mm-long PPLNOI waveguide.[29] It is important to note that there is an upper limit of conversion efficiency in theory for PPLNOI devices pumping at telecommunication wavelength, which is around 5000% $\text{W}^{-1}\,\text{cm}^{-2}$, depending on the specific configurations in PPLNs.[28] In addition, birefringent phase-matching (BPM) in an x-cut LNOI has been demonstrated, but η_{norm} (2.7% $\text{W}^{-1}\,\text{cm}^{-2}$) is constrained by the low nonlinear susceptibility ($d_{31} \sim 4.7$ pm/V) inevitably used when both polarization states interact with each other.[30] Another competent approach that keeps making progress is modal phase matching (MPM).[31] Initially, the poor modal overlap between modes of different orders in the MPM generally results in low conversion efficiency.[32,33] To solve this problem, researchers have modified the $\chi^{(2)}$ profile in the waveguide cross section to improve the modal overlap, including chemically changing $\chi^{(2)}$ by ion exchange[34,35] or coating the waveguide with a material with $\chi^{(2)} = 0$,[36,37] exhibiting enhanced conversion efficiency compared to the conventional MPM. However, in these methods, $\chi^{(2)}$ in part of the waveguide core region is zero and has no contribution to the SHG process. To solve this issue, a polarization-reversed double-layer LNOI waveguide with reconfigured $\chi^{(2)}$ profile[38,39] is proposed to fully leverage the high nonlinear coefficient of LN and achieve η_{norm} of 5540% $\text{W}^{-1}\,\text{cm}^{-2}$, which is already comparable to the highest achievable η_{norm} of PPLNOI waveguides.[28] Nevertheless, it is still highly desirable to enable significantly higher conversion efficiency toward its theoretical limit for MPM-based LNOI SHG devices.

Here, we demonstrate SHG with an unprecedented conversion efficiency in a double-layer x-cut LNOI waveguide by MPM. Our model reveals that, with the realistic waveguide properties enabled in advanced nanofabrication, an achievable conversion efficiency can be close to the theoretical limit. A record-high η_{norm} of 9600% $\text{W}^{-1}\,\text{cm}^{-2}$ is obtained, 2 times higher than that given by PPLNOIs, while η_{abs} is as high as 85%. Such a highly efficient frequency converter also exhibits tunability of 0.071 nm/K by the thermal-optic effect of LN. These results pave the way for developing a variety of on-chip frequency converters with ultrahigh efficiency in frequency metrology, quantum optics, and ultrafast optics.

2 Device Design and Fabrication

To achieve an efficient SHG, the phase matching (PM) condition should be satisfied,[1] which implies

$$k_{2\omega} = 2k_{\omega}, \tag{1}$$

where k_{ω} and $k_{2\omega}$ are the wave vectors at fundamental and second-harmonic (SH) frequencies, respectively. Due to the relation of $k = n\omega/c$, Eq. (1) indicates that one needs to find fundamental and SH modes with identical effective refractive indices ($n_{\omega} = n_{2\omega}$). Considering the material and waveguide dispersions, this condition can be fulfilled by selecting the fundamental mode at ω and higher-order mode at 2ω in MPM.

To utilize the largest component of the second-order nonlinear tensor ($d_{zzz} = d_{33} = 25$ pm/V), TE_{00} mode at the fundamental wavelength and TE_{01} mode at SH wavelength in an x-cut LNOI waveguide are chosen. The cross section of the double-layer LNOI waveguide is shown in Fig. 1(a). The waveguide has a device-layer thickness, H, of 500 nm ($h_1 = h_2 = 250$ nm), a top width, w, of 850 nm, an etching depth, h, of 450 nm, and a sidewall angle, θ, of 66.5 deg.

The finite element method is used for calculating the properties of waveguide eigenmodes, including their effective refractive indices and mode profiles, based on which we can access the PM condition and modal overlap. To evaluate SHG power and conversion efficiency, especially in a high-power regime where an analytical solution is unavailable, we use numerical calculation based on the formula below[21]

$$\frac{\partial A_{\text{SH}}}{\partial y} = -\frac{\alpha_{\text{SH}}}{2}A_{\text{SH}} - i\kappa_{\text{SH}}A_f^2\,\exp[i\Delta k y], \tag{2}$$

$$\frac{\partial A_f}{\partial y} = -\frac{\alpha_f}{2}A_f - i\kappa_f A_{\text{SH}}A_f^*\,\exp[-i\Delta k y], \tag{3}$$

where α_{SH} and α_f are the waveguide propagation losses at fundamental and SH wavelengths, respectively. A is proportional to the amplitude of the interacting light. The coupling coefficients are

$$\kappa_{\text{SH}} = \frac{d_{33}\omega_{\text{SH}}}{\pi c n_{\text{SH}}} \bullet \frac{\iint E_f^2(x,z)E_{\text{SH}}(x,z)\text{d}x\,\text{d}z}{\iint E_{\text{SH}}^2(x,z)\text{d}x\,\text{d}z}, \tag{4}$$

$$\kappa_f = \frac{2d_{33}\omega_f}{\pi c n_f} \bullet \frac{\iint E_f^2(x,z)E_{\text{SH}}(x,z)\text{d}x\,\text{d}z}{\iint E_f^2(x,z)\text{d}x\,\text{d}z}, \tag{5}$$

the phase mismatch Δk is

$$\Delta k = k_{\text{SH}} - 2k_f. \tag{6}$$

The SH power $P_{2\omega}$ generated by a device with waveguide length L can be expressed as

$$P_{2\omega} = \eta_{\text{norm}}L^2P_{\omega}^2 g(L), \tag{7}$$

where P_{ω} is the pump power and

$$\eta_{\text{norm}} = \frac{8d_{33}^2}{\varepsilon_0 c n_{\text{SH}} n_f^2 \lambda_{\text{SH}}^2 S_{\text{eff}}}\,\text{sinc}^2\left(\frac{\Delta k L}{2}\right) \tag{8}$$

is the normalized efficiency expressed in $\text{W}^{-1}\,\text{cm}^{-2}$, where d_{33} is the nonlinear coefficient of the material, ε_0 is the vacuum permittivity, c is the speed of light in vacuum, and n_{ω} and $n_{2\omega}$ are the effective refractive indices for the fundamental mode and the SH mode, respectively. S_{eff} can be expressed as

$$S_{\text{eff}} = \frac{[\iint E_f^2(x,z)\text{d}x\,\text{d}z]^2 \iint E_{\text{SH}}^2(x,z)\text{d}x\,\text{d}z}{[\iint E_f^2(x,z)E_{\text{SH}}(x,z)\text{d}x\,\text{d}z]^2}, \tag{9}$$

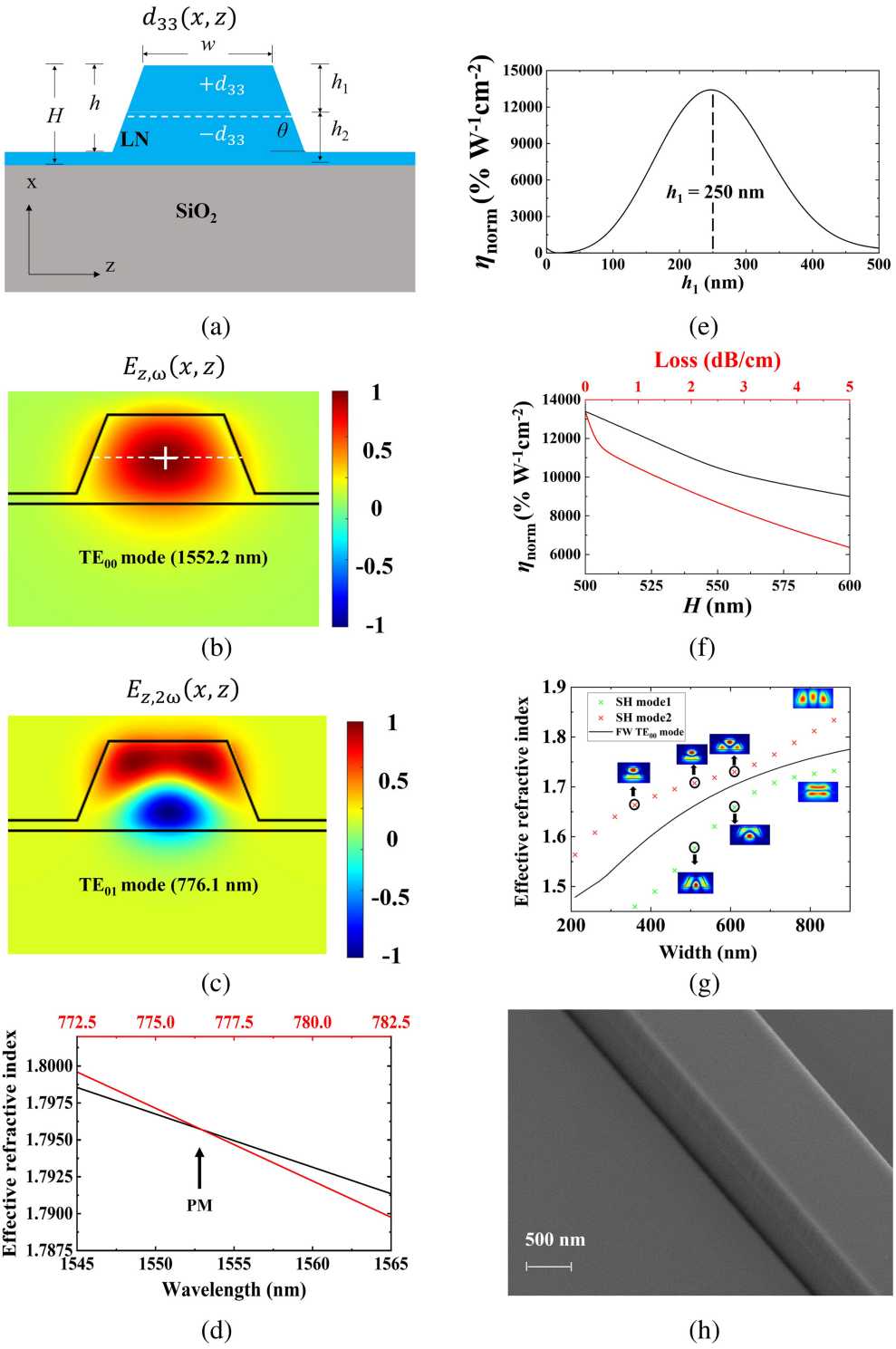

Fig. 1 (a) Schematic of the waveguide cross section. (b) Dominant electric field component (E_z) of the TE_{00} mode at the fundamental wavelength. (c) Dominant electric field component (E_z) of the TE_{01} mode at the SH wavelength. Both d_{33} and E_z of the TE_{01} mode have the opposite signs across the polarization-reversed double-layer LN. (d) Dependence of the effective refractive indices of the interacting waveguide modes on wavelength, with PM at 1552.2 nm. (e) Calculated η_{norm} of the double-layer LNOI waveguide as a function of h_1. (f) Black: η_{norm} versus the total thickness (H) of the waveguide. Red: η_{norm} versus the waveguide loss. (g) Effective refractive indices of the interacting waveguide modes versus the width of the waveguide when H is 450 nm. (h) Scanning electron microscopy (SEM) image of the waveguide sidewall.

where $E(x,z)$ is the spatial mode profile of transverse waveguide modes. S_{eff} mainly depends on the mode size at the different wavelengths and the overlap between them. Finally, the loss factor $g(L)$ is expressed as

$$g(L) = e^{-2\alpha_f L}\frac{(e^{\Delta\alpha L}+1)^2 - 4\cos^2\left(\frac{\Delta kL}{2}\right)e^{\Delta\alpha L}}{\Delta\alpha^2+\Delta k^2}, \tag{10}$$

where

$$\Delta\alpha = \alpha_f - \frac{\alpha_{\text{SH}}}{2}. \tag{11}$$

The effective refractive indices of these two modes as a function of wavelength are calculated and shown in Fig. 1(d). The PM is achieved at the wavelength of 1552.2 nm. Figures 1(b) and 1(c) show the dominant electric field component (E_z) of the TE_{00} mode at 1552.2 nm and TE_{01} mode at 776.1 nm, respectively. The conversion efficiency of SHG highly depends on the modal overlap (Γ)

$$\Gamma = \iint_{\text{LN}} d_{33}(x,z)E^2_{z,\omega}(x,z)E_{z,2\omega}(x,z)\mathrm{d}x\,\mathrm{d}z. \tag{12}$$

Since the electric field of the TE_{01} mode changes its sign across the waveguide core, as shown in Fig. 1(c), the positive and negative contributions to the integral almost cancel out, and the resulting Γ is generally small. Methods of enhancing Γ reported in previous works include introducing a double-ridge waveguide[31] and modifying $\chi^{(2)}$ profile.[34–37] Here, by introducing a polarization-reversed double-layer structure [see d_{33} distribution in Fig. 1(a)], the nonlinear coefficient d_{33} has the opposite signs as well across the waveguide, leading to a significant enhancement of Γ and resolving the fundamental issue in the MPM scheme. Figure 1(e) shows that η_{norm} reaches a maximum value when the two LN layers have approximately equal thicknesses.

Previous works investigated the SHG process in double-layer LNOI for device-layer thicknesses larger than 550 nm and conducted experiments with a thickness of 570 nm.[39] In fact, η_{norm} depends on waveguide geometry, and we find that smaller thickness leads to higher η_{norm} [see Fig. 1(f)] because of more compact mode sizes, but mode hybridization makes PM difficult when the thickness is smaller than ~500 nm [see a case for $H = 450$ nm in Fig. 1(g), in which two SH modes hybridize and PM condition is not satisfied for any widths]. Therefore, an LN thickness of 500 nm is chosen in this work to reach a relatively high η_{norm} and ensure that the PM condition can be accessed.

Waveguides are fabricated on an x-cut double-layer LNOI with a 2-μm-thick buried oxide.[39] First, a layer of negative electron-beam resist is spin-coated as the etching mask, and device patterns are defined by electron-beam lithography. The acceleration voltage and beam current used in the electron-beam lithography are 100 kV and 1 nA, respectively. Then, the patterns are transferred to LN by argon plasma etching in an inductively coupled plasma reactive ion etching (ICP-RIE) tool (Oxford Instruments PlasmaPro 100 Cobra) with the following parameters: Ar flow of 15 sccm, DC bias of 190 V, ICP power of 1000 W, and pressure of 2 mTorr. The etching depth is measured to be 450 nm. We preserve a 50-nm-thick unetched LN layer to prevent the buried oxide from etching by the hydrofluoric acid in the following cleaning step. As shown in Fig. 1(h), the waveguide sidewall is smooth, indicating high fabrication quality and low scattering loss from the roughness of the sidewalls. The total waveguide length, L, is 10 mm.

3 Optical Characterization

The measurement setup is shown in Fig. 2. Pump light from a continuous-wave tunable laser (Santec TSL-570) is coupled into the waveguide using a lensed fiber. We use an in-line fiber polarization controller to ensure TE polarization at the input. When the pump laser is tuned to the PM wavelength, strong SH light is observed at the waveguide output facet. An SHG signal is collected using an aspheric lens (numerical aperture is 0.5) and detected by a photodetector (Thorlabs S130C). When measurement is performed under high-power pumping conditions, an erbium-doped fiber amplifier (EDFA) is used to boost the pump light.

By scanning the laser wavelength, we measure the dependence of the SHG signal on wavelength. Taking into account the measured fiber-to-chip coupling loss (around 8 dB per facet) and assuming that the SHG signal generated in the waveguide is completely collected by the lens, the pump power (P_ω) at the input facet and the SHG power ($P_{2\omega}$) at the output facet of the waveguide can be determined. Then, η_{norm} is calculated according to the formula: $\eta_{\text{norm}} = P_{2\omega}/(P_\omega L)$.[2] We plot η_{norm} as a function of wavelength in Fig. 3(a). Maximum η_{norm} of 9600% $\text{W}^{-1}\text{cm}^{-2}$, 8845%$\text{W}^{-1}\text{cm}^{-2}$, and 9013% $\text{W}^{-1}\,\text{cm}^{-2}$ are obtained at PM wavelengths of 1485.7, 1518.3, and 1552.2 nm for three waveguides with different widths, respectively. To the best of our knowledge, these are the highest η_{norm} reported in LN or LNOI waveguides pumped around the telecommunication band, indicating the advantage of MPM implemented in double-layer LNOI over QPM as well as the high fabrication quality of the SHG waveguides. The discrepancies of the maximum η_{norm} between experiment and simulation with an ideal model can be attributed to the waveguide propagation loss. By fabricating a microring resonator with the same waveguide geometry as that used for SHG, and with a sufficiently large radius of 200 μm to avoid additional scattering and bend

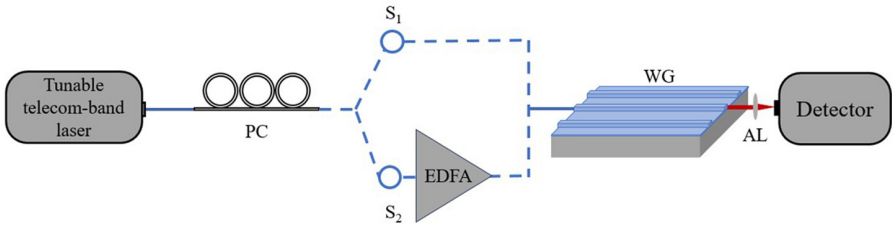

Fig. 2 Experimental setup for device characterization. PC, polarization controller; EDFA, erbium-doped fiber amplifier; WG, waveguide; AL, aspherical lens.

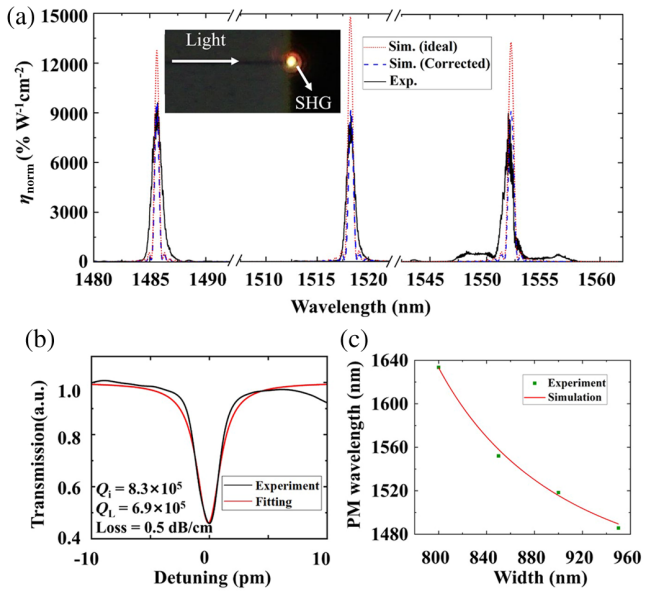

Fig. 3 (a) Measured η_{norm} (black) as a function of wavelength. Maximum η_{norm} of 9600% W^{-1} cm^{-2} at 1485.7 nm is observed. The red dotted and blue dashed curves correspond to simulations with ideal and corrected models, respectively. The inset shows the top-view optical micrograph of the scattered SH signal at the waveguide facet. (b) The transmission spectrum of a microring resonator is used to extract waveguide loss, with experimental data shown in black and a fitting curve shown in red. (c) PM wavelength versus the top width of the waveguide.

losses, the intrinsic quality factor and the corresponding waveguide loss are extracted to be 8.3×10^5 and 0.5 dB/cm at 1550 nm, respectively [as shown in Fig. 3(b)]. Compared with the previous work of SHG in double-layer LNOI ($\eta_{\text{norm}} = 5540\%$ W^{-1} cm^{-2} with a propagation loss of 3.8 dB/cm),[39] the lower loss achieved in this work can contribute to the improvement of the measured conversion efficiency. Taking into account the waveguide loss at the fundamental wavelength and the unequal thicknesses of the two LN layers ($h_1 = 220$ nm and $h_2 = 280$ nm measured by SEM) and assuming that the waveguide loss at SH wavelength is 0.8 dB/cm in our simulation model, the measured spectra (black curves) are consistent with those of the corrected model (blue dashed curves). PM wavelengths extracted from Fig. 3(a) and the corresponding simulated results can be found in Fig. 3(c). The inset in Fig. 3(a) is the top-view optical micrograph of the scattered SH signal at the waveguide facet.

By fixing the pump wavelength at 1552.2 nm for the maximum η_{norm}, the SHG power is recorded as a function of the pump power, as shown in Fig. 4. As expected, in the low-power regime [$P_\omega < 0.7$ mW in the inset of Fig. 4(a)], their relation basically follows a quadratic dependence of an SHG process without pump depletion. We use an EDFA to further increase the pump power and investigate the device behavior under high-power pumping conditions. The measured SHG power is consistent with that simulated with pump depletion and waveguide propagation loss. We extract the η_{abs}, defined as $\eta_{\text{abs}} = P_{2\omega}/P_\omega$, from Fig. 4(a) and find that η_{abs} starts to saturate when P_ω is higher than 80 mW [Fig. 4(b)]. Notably, η_{abs} in our work reaches an unprecedented value of 85% among the SHG waveguides reported in LNOI, simultaneously possessing the record-high η_{norm}, as illustrated in Fig. 3.

LN exhibits a significant thermo-optic effect for extraordinary light on the order of 10^{-5}, while it is negligible for ordinary light, given by the following equations:

$$\frac{\mathrm{d}n_{e,\mathrm{FW}}}{\mathrm{d}T} = -2.6 + 19.8\times10^{-3}T, \tag{13}$$

$$\frac{\mathrm{d}n_{e,\mathrm{SH}}}{\mathrm{d}T} = -2.6 + 22.4\times10^{-3}T. \tag{14}$$

These equations are reliable in a temperature range from 300 to 515 K.[40,41] As a result, a temperature change would lead to an index change of LN and hence shift the PM wavelength of the SHG process. We leverage the thermo-optic effect in LN to achieve a tunable SHG device. The sample is mounted on a

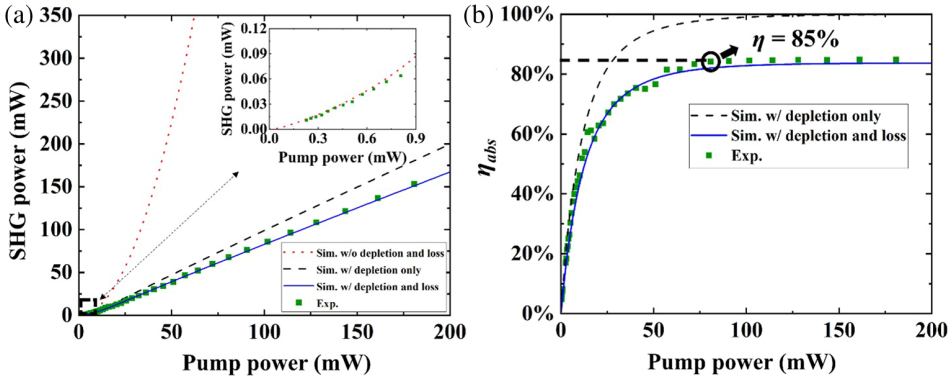

Fig. 4 (a) Measured (green) and simulated dependence of SHG power (at the output facet of the waveguide) on the pump power (at the input facet of the waveguide). Red dashed line: simulation without considering pump depletion and waveguide loss. Black dashed line: simulation with considering pump depletion only. Blue dashed line: simulation with considering both pump depletion and waveguide loss. The inset shows the input–output power relation in the low-power regime. (b) Measured and simulated η_{abs} ($\eta_{\text{abs}} = P_{2\omega}/P_\omega$) of SHG as a function of the pump power extracted from (a).

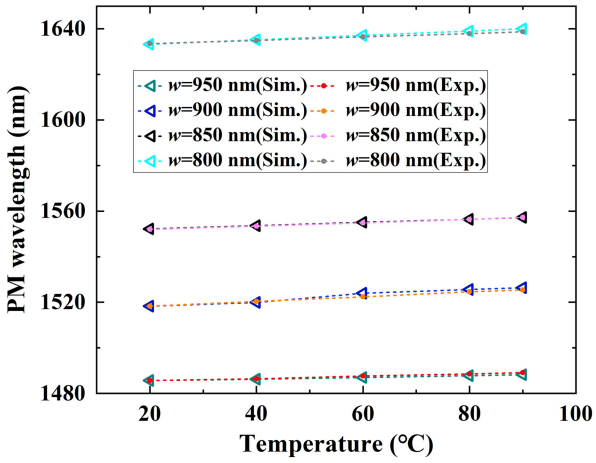

Fig. 5 Measured and simulated PM wavelengths as a function of temperature, in good agreement. Also, this exhibits a desirable thermal tunability.

thermoelectric cooler and its temperature is changed by a temperature controller. Figure 5 shows the simulated and measured PM wavelengths at various temperatures. The PM condition moves toward longer wavelengths as temperature increases. The extracted tunability of our SHG device, 0.071 nm/K, agrees well with the simulated value.

Finally, we compare the LNOI waveguides for SHG at the telecommunication band, including MPM, QPM, and BPM schemes, in terms of the waveguide length, pump power, η_{abs} (in the unit of %), η_{SHG} (in the unit of $\%W^{-1}$), η_{norm} (in the unit of $\%W^{-1}\,cm^{-2}$), and SH power, as presented in Table 1.

By equalizing the thicknesses of the two LN layers and further reducing propagation loss, possibly down to 0.2 dB/cm, one can expect that the normalized conversion efficiency can be improved to 11,700% $W^{-1}\,cm^{-2}$.

On the other hand, it is noteworthy that an optical microresonator can enhance the SHG efficiency in both QPM and MPM schemes,[42] and an extremely high efficiency of 5,000,000% W^{-1} has been reported.[43] However, it is believed that the waveguide-based SHG process exhibits unique advantages, such as large bandwidth, high absolute conversion efficiency, wide tunability, and good tolerance of fabrication errors, which are highly desirable in practice.

4 Conclusion

In conclusion, highly efficient SHG in a double-layer LNOI waveguide is demonstrated. Leveraging the significantly enhanced modal overlap in the polarization-reversed LN layers and the high-quality nanofabrication, an on-chip normalized conversion efficiency as high as 9600% $W^{-1}\,cm^{-2}$ is achieved, associated with an absolute conversion efficiency of 85% when pumping around 1552.2 nm. Our results outperform other works on MPM[31] and lend strong support to the competitiveness of the MPM scheme in such a new platform for a variety of nonlinear applications when compared to previously reported methods such as PPLN. The presented results pave the way for efficient nonlinear wave-mixing processes for classical and quantum applications.

Code and Data Availability

The code and data that support the findings of this study are available from the corresponding author upon reasonable request.

Acknowledgments

We acknowledge support from the Advanced Integrated Optoelectronics Facility at Tianjin University.

References

1. R. W. Boyd, *Nonlinear Optics*, Academic Press, San Diego, California (2020).
2. Y. Okawachi et al., "Chip-based self-referencing using integrated lithium niobate waveguides," *Optica* **7**(6), 702–707 (2020).
3. F. Mondain et al., "Chip-based squeezing at a telecom wavelength," *Photonics Res.* **7**(7), A36–A39 (2019).
4. D. D. Arslanov et al., "Continuous-wave optical parametric oscillator based infrared spectroscopy for sensitive molecular gas sensing," *Laser Photonics Rev.* **7**(2), 188–206 (2013).

Table 1 Comparison of SHG waveguides in LNOI working at telecommunication band.

Platform	PM type	Length (mm)	Pump power (mW)	η_{abs} (%)	η_{SHG} ($\%W^{-1}$)	η_{norm} ($\%W^{-1}\,cm^{-2}$)	SH power (mW)
PPLNOI[21]	QPM	5	NA	NA	40[a]	160	NA
PPLNOI[22]	QPM	4	220	53	416[a]	2600	117
PPLNOI[28]	QPM	0.6	NA	NA	16.6[a]	4600	NA
PPLNOI[29]	QPM	21	20	82.5	9500	2154	16.5
LNOI[30]	BPM	20	25[a]	0.3[a]	10.7	2.7	0.067[a]
LNOI[32]	MPM	8	NA	NA	4.7	7.4	NA
LNOI[33]	MPM	0.9	0.737	4.5×10^{-5}[a]	0.06	6.9	3.05×10^{-7}
LNOI[34]	MPM	3.2	NA	NA	5[a]	48	NA
LNOI[36]	MPM	2.35	NA	NA	36	650	NA
LNOI[39]	MPM	1.2	0.126[a]	0.01[a]	79.8	5540	1.26×10^{-5}[a]
LNOI (this work)	**MPM**	**10**	**200**	**85**	**9600**	**9600**	**170**

NA, data not available.
[a]The value was calculated according to the data in reference.

5. T. H. Wu et al., "Visible-to-ultraviolet frequency comb generation in lithium niobate nanophotonic waveguides," *Nat. Photonics* **18**(3), 218–223 (2024).
6. A. Boes et al., "Lithium niobate photonics: unlocking the electromagnetic spectrum," *Science* **379**(6627), eabj4396 (2023).
7. C. Langrock et al., "All-optical signal processing using $\chi^{(2)}$ nonlinearities in guided-wave devices," *J. Lightwave Technol.* **24**(7), 2579–2592 (2006).
8. K. R. Parameswaran et al., "Highly efficient second-harmonic generation in buried waveguides formed by annealed and reverse proton exchange in periodically poled lithium niobate," *Opt. Lett.* **27**(3), 179 (2002).
9. F. Thiele et al., "Cryogenic electro-optic polarisation conversion in titanium in-diffused lithium niobate waveguides," *Opt. Express* **28**(20), 28961 (2020).
10. D. Zhu et al., "Integrated photonics on thin-film lithium niobate," *Adv. Opt. Photonics* **13**(2), 242 (2021).
11. R. Gao et al., "Lithium niobate microring with ultra-high Q factor above 10^8," *Chin. Opt. Lett.* **20**(1), 011902 (2022).
12. B. Pan et al., "Perspective on lithium-niobate-on-insulator photonics utilizing the electro-optic and acousto-optic effects," *ACS Photonics* **10**(7), 2078–2090 (2023).
13. M. He et al., "High-performance hybrid silicon and lithium niobate Mach–Zehnder modulators for 100 Gbit s^{-1} and beyond," *Nat. Photonics* **13**(5), 359–364 (2019).
14. Z. Zhang et al., "Erbium-ytterbium codoped thin-film lithium niobate integrated waveguide amplifier with a 27 dB internal net gain," *Opt. Lett.* **48**(16), 4344 (2023).
15. L. Shao et al., "Integrated microwave acousto-optic frequency shifter on thin-film lithium niobate," *Opt. Express* **28**(16), 23728 (2020).
16. M. G. Vazimali and S. Fathpour, "Applications of thin-film lithium niobate in nonlinear integrated photonics," *Adv. Photonics* **4**(3), 034001 (2022).
17. M. D. Eisaman et al., "Invited review article: single-photon sources and detectors," *Rev. Sci. Instrum.* **82**(7), 071101 (2011).
18. X. Guo et al., "Parametric down-conversion photon-pair source on a nanophotonic chip," *Light Sci. Appl.* **6**(5), e16249 (2016).
19. D. T. Spencer et al., "An optical-frequency synthesizer using integrated photonics," *Nature* **557**(7703), 81–85 (2018).
20. N. Jornod et al., "Monolithically integrated femtosecond optical parametric oscillators," *Optica* **10**(7), 826 (2023).
21. L. Chang et al., "Thin film wavelength converters for photonic integrated circuits," *Optica* **3**(5), 531 (2016).
22. C. Wang et al., "Ultrahigh-efficiency wavelength conversion in nanophotonic periodically poled lithium niobate waveguides," *Optica* **5**(11), 1438 (2018).
23. J. Zhao et al., "Shallow-etched thin-film lithium niobate waveguides for highly-efficient second-harmonic generation," *Opt. Express* **28**(13), 19669 (2020).
24. X. Liu et al., "Ultra-broadband and low-loss edge coupler for highly efficient second harmonic generation in thin-film lithium niobate," *Adv. Photonics Nexus* **1**(1), 016001 (2022).
25. J. Wei et al., "All-optical wavelength conversion of a 92-Gb/s 16-QAM signal within the C-band in a single thin-film PPLN waveguide," *Opt. Express* **30**(17), 30564 (2022).
26. K. Mizuuchi et al., "Electric-field poling in Mg-doped $LiNbO_3$," *J. Appl. Phys.* **96**(11), 6585–6590 (2004).
27. Y. Niu et al., "Optimizing the efficiency of a periodically poled LNOI waveguide using in situ monitoring of the ferroelectric domains," *Appl. Phys. Lett.* **116**(10), 101104 (2020).
28. A. Rao et al., "Actively-monitored periodic-poling in thin-film lithium niobate photonic waveguides with ultrahigh nonlinear conversion efficiency of 4600% W^{-1} cm^{-2}," *Opt. Express* **27**(18), 25920–25930 (2019).
29. P.K. Chen et al., "Adapted poling to break the nonlinear efficiency limit in nanophotonic lithium niobate waveguides," *Nat. Nanotechnol.* **19**(1), 44–50 (2024).
30. C. Lu et al., "Highly tunable birefringent phase-matched second-harmonic generation in an angle-cut lithium niobate-on-insulator ridge waveguide," *Opt. Lett.* **47**(5), 1081 (2022).
31. M. T. Hansen et al., "Efficient and robust second-harmonic generation in thin-film lithium niobate using modal phase matching," *Front. Photonics* **4**, 1324648 (2023).
32. R. Luo et al., "Highly tunable efficient second-harmonic generation in a lithium niobate nanophotonic waveguide," *Optica* **5**(8), 1006 (2018).
33. R. Geiss et al., "Fabrication of nanoscale lithium niobate waveguides for second-harmonic generation," *Opt. Lett.* **40**(12), 2715 (2015).
34. L. Cai, Y. Wang, and H. Hu, "Efficient second harmonic generation in $\chi^{(2)}$ profile reconfigured lithium niobate thin film," *Opt. Commun.* **387**, 405–408 (2017).
35. L. Cai et al., "Highly efficient broadband second harmonic generation mediated by mode hybridization and nonlinearity patterning in compact fiber-integrated lithium niobate nano-waveguides," *Sci. Rep.* **8**(1), 12478 (2018).
36. R. Luo et al., "Semi-nonlinear nanophotonic waveguides for highly efficient second-harmonic generation," *Laser Photonics Rev.* **13**(3), 1800288 (2019).
37. X. Li et al., "Efficient second harmonic generation by harnessing bound states in the continuum in semi-nonlinear etchless lithium niobate waveguides," *Light Sci. Appl.* **11**(1), 317 (2022).
38. H. Du et al., "Highly efficient, modal phase-matched second harmonic generation in a double-layered thin film lithium niobate waveguide," *Opt. Express* **31**(6), 9713 (2023).
39. L. Wang, X. Zhang, and F. Chen, "Efficient second harmonic generation in a reverse-polarization dual-layer crystalline thin film nanophotonic waveguide," *Laser Photonics Rev.* **15**(12), 2100409 (2021).
40. D. E. Zelmon, D. L. Small, and D. Jundt, "Infrared corrected Sellmeier coefficients for congruently grown lithium niobate and 5 mol % magnesium oxide–doped lithium niobate," *J. Opt. Soc. Amer. B* **14**(12), 3319–3322 (1997).
41. L. Moretti et al., "Temperature dependence of the thermo-optic coefficient of lithium niobate, from 300 to 515 K in the visible and infrared regions," *J. Appl. Phys.* **98**(3), 036101 (2005).
42. X. Guo, C. Zou, and H. X. Tang, "Second-harmonic generation in aluminum nitride microrings with 2500% /W conversion efficiency," *Optica* **3**(10), 1126 (2016).
43. J. Lu et al., "Toward 1% single-photon anharmonicity with periodically poled lithium niobate microring resonators," *Optica* **7**(12), 1654 (2020).

Biographies of the authors are not available.